BeBeC-2026-D10

SOURCE LOCALIZATION AROUND A SHORT CYLINDER IN FLOW USING CROSS-SHAPED BEAMFORMING

Hugo Demontis[1] and Laurent Sanders
[1]DAAA, ONERA, Institut Polytechnique de Paris
93320, Châtillon, France

Abstract

The acoustic field generated by a short cylinder immersed in a subsonic flow, representative of a simplified isolated landing gear wheel, is investigated by coupling a high-fidelity aeroacoustic computational chain with state-of-the-art phased-array processing techniques. The acoustic data are synthetized using two complementary numerical approaches: a direct solution of the lattice-Boltzmann method, and a porous formulations of the Ffowcs-Williams & Hawkings surface integral. These simulations yield time-resolved pressure signals over two cross-shaped arrays in the far field of the cylinder, respectively a horizontal array above and a vertical array on its side. An adaptive beamforming algorithm is then implemented, by exploiting the cross geometry of the arrays, in order to generate high-resolution source power maps around the cylinder. This work also examines the choice of the numerical method, between direct noise from lattice-Boltzmann solver or surface integral, and its influence for the reconstruction of the source distribution by the two array configurations.

1 INTRODUCTION

Over decades of scientific research and development aimed at designing low-noise turbofan engines, the airframe noise has become more noticeable, particularly during low-speed flight phases like approach and landing. Among all existing types of airframe noise sources, the landing gear is known to contribute the most to commercial aircraft noise. This can be explained by the geometry of the landing gear systems, characterized by multiple unstreamlined elements (tires, struts, locks, wiring) which produces local and complex unsteady flow interactions with the overall structure [17].

Experimental investigation of landing gear noise at different scale has been extensively conducted in wind tunnels of various size [3, 9, 10, 12, 14], in order to thoroughly test all possible

configurations for landing gears and to measure the resulting far-field noise spectra. Building an exhaustive and accurate noise database is required to develop and validate new dedicated numerical methods. In this context, microphone array processing is an interesting tool to visualize the noise source distribution on the different parts of the landing gear and thus, rapidly giving valuable information about their individual emitted noise level. This approach has been applied by Humphreys and Brooks to study a scale model of langing gear of a long range widebody aircraft [9]. The authors used the conventionnal beamforming and the deconvolution algorithm DAMAS to estimate acoustic maps for four different configurations of the model and, by direct comparison between them, to evaluate a proposed noise reduction concept. The microphone array is also moved at fixed polar and azimuthal angles around the landing gear to measure its directivity. Bulte and Redonnet [5] have also used source localization algorithms on a simplified two-wheel nose landing gear, highlighting the sound source distribution focused around the axle and the wheels.

Microphone array processing is also useful to analyze computational data derived from high-fidelity aeroacoustic simulation. As also proposed in [5], the authors compared the deconvolved cartographies obtained using numerical and experimental data for a similar configuration of landing gear, showing good agreements for both in term of power spectral density estimation. Recently, Bouley et al. [4] applied high-resolutive array processing, the so-called CLEAN-SC algorithm and an iterative Bayesian focusing technique, to identify noise sources over the LAGOON benchmark. Here, the acoustic signals for a spherical distribution of microphones around the landing gear are computed as the direct noise solution of a lattice-Boltzmann solver. The main advantage of computational aeroacoustics over wind tunnel facilities is the ability to test complex and proteiformic array geometries at a lower cost, and even to optimize dedicated instrumentation for specific noise prior to their deployment. Furthermore, as noted by the authors, the absence of spurious sources associated with the installation of acoustic sensors, like echos or background noise, allows for better recovering of noise sources, provided that these are simulated with a sufficient degree of fidelity.

This paper deals with the simulation of landing gear noise and the analysis of its far-field radiation using acoustic antenna techniques. It is a preliminary work aimed at better understanding the noise sources generated by each individual component of the landing gear, rather than treating it as a entire complex system. Therefore, only an isolated wheel, represented as a simplified short cylinder geometry immersed in subsonic uniform flow, is considered. At first, the computational pipeline implemented to generate time-resolved pressure data all around the wheel is described. A new formulation of the conventional beamforming, which makes use of the cross-shaped arrangement of sensors, is then formulated. The method is finally applied over several synthetic datasets in order to retrieve the source distribution near the wheel. A discussion is proposed about the quality of source identification depending on the numerical methods in used.

2 AEROACOUSTIC COMPUTATIONAL SETUP

2.1 Configuration

Figure 1 shows the short cylinder geometry used for the present study. It is a simplification of a landing gear wheel at scale 1:4. With a diameter $D = 0.263$ m and a span $W = 0.106$ m, the

aspect ratio equals $W/D \approx 0.4$. The round radius on the sides of the cylinder is $r = 0.032$ m. Around the cylinder, the flow field moves at constant velocity $U = 80$ m/s leading to a high Reynolds number of 1.4×10^6.

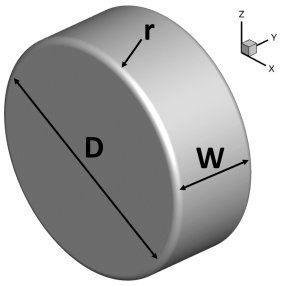

Figure 1: Short cylinder geometry.

2.2 Numerical Approach

The lattice-Boltzmann method offers interesting trade-off between accuracy and CPU cost for aeroacoustic applications [15]. Here, the flow simulation is achieved with the LBM implemented in the ProLB solver[1]. A D3Q19 lattice is used to compute the distribution functions. As for the collision model, a Hybrid Recursive Regularized approach is used [11]. It includes some corrections to cancel high order (M^3) terms leading to a more robust code under high Mach number, while remaining athermal. As for the turbulence, a shear-improved Smagorinsky model [13] is used here. Solid surfaces are defined by means of immersed boundary conditions and the fluid boundary layer is resolved thanks to an advanced wall log-law which account for adverse pressure gradient [1] and curvature effect. A Direct Coupling approach is used to drastically reduced the spurious noise generated at change of resolution since the present LBM method makes use of octree grid [2].

2.3 Numerical set-up

The fluid simulation domain is $180D$ long and $170D$ wide and high. The flow velocity U is imposed at the inlet and a pressure condition is prescribed at the outlet and all other boundary conditions. The cylinder has a no-slip condition associated to the wall log-law. In addition, absorbing layers are included in far-field to damp acoustical waves before they exit the computational domain and avoid spurious backscattered acoustic fields.

In the far-field, the cell size is $0.48D$ whereas the mesh is refined at the cylinder wall and in the cylinder wake. At the cylinder wall, the cell size is $\Delta x = r/256$. At the cylinder wake, up to a length of $2D$ behind the end of the cylinder, the cell size is $4\Delta x$, see Figure 2.

2.4 Aerodynamic Results

Figure 3 shows the y^+ values, lower than 50, on the cylinder skin. This is in agreement with the expected values for the correct use of the wall model given the strong pressure gradients around

[1] https://www.prolb-cfd.com/

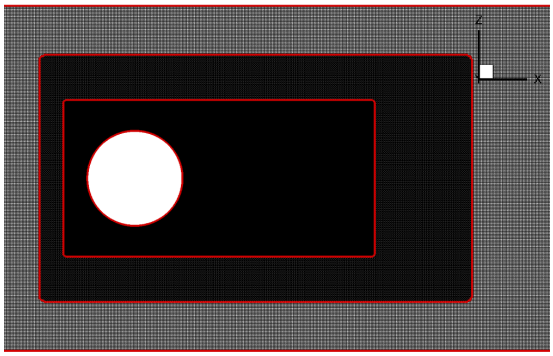

Figure 2: Mesh refinement around the cylinder and along its wake.

the geometry. Figure 4 gives some insights into the flow topology. Turbulent structures are generated on the sides of the cylinder and downstream of its end (Fig. 4a). Two antisymmetric pairs of vortices are created in the wake, the traces of which are visible on the surface of the cylinder (Fig. 4b). The kinetic energy shows slightly more intense fluctuations on the side of the cylinder than in its wake (Fig. 4c).

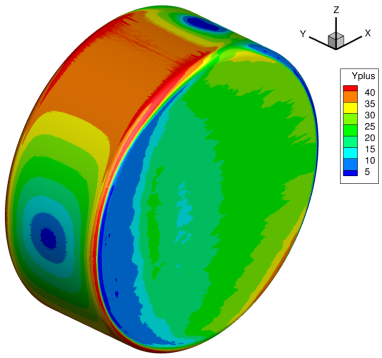

Figure 3: y^+ values on the cylinder skin.

2.5 Acoustic Results

The acoustic computations employ two distinct approaches. First, owing to a dedicated mesh refinement in mid-field, the direct noise from the LBM flow simulation is accurately propagated throughout the entire volume up to Strouhal number $St_D = 40.3$ ($f = 12.3$ kHz), corresponding to a full-scale frequency of approximately 3 kHz. The second approach utilizes a Ffowcs Williams-Hawkings (FW-H) surface integral over a permeable surface surrounding the cylinder and its wake, as illustrated in Fig. 5a. An hemisphere of mid-field microphones with a radius of $3.8D$ is also defined to facilitate data comparison across the different computations. In terms of acoustic waves, frequencies above 1.8 kHz ($R \geq 5\lambda$) can be considered in far-field.

Figure 5b shows the Power Spectral Density (PSD) comparison on microphone n°127 (indicated by a red marker in Fig. 5a) for the two acoustic computations. The direct noise exhibits a lower spectral cut-off due to mesh-induced dissipation, as expected. For the permeable surface,

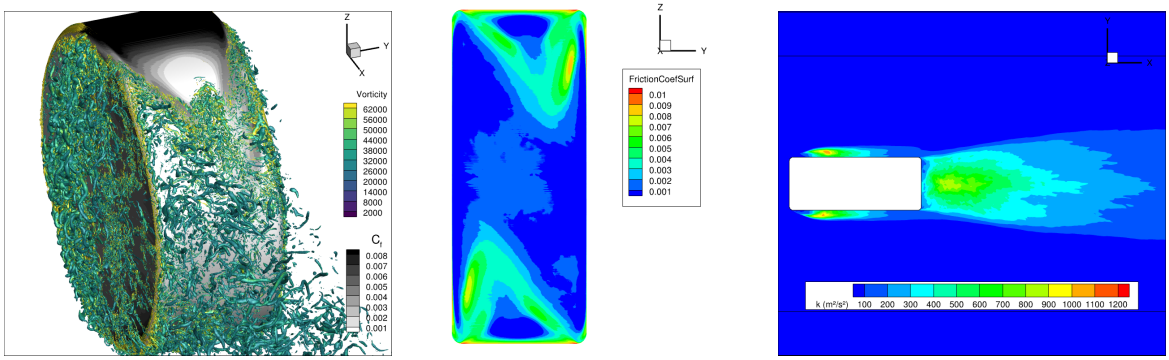

(a) (b) (c)

Figure 4: Insights of the flow topology.

computations were performed without the end surface closure. Based on comparisons with other microphones (not shown for brevity), the open permeable surface demonstrates overall good agreement with the direct noise for broadband frequencies. The upper frequency limit of the compacity of the cylinder is around $1.3 - 3.2$ kHz, based on a $M_0 St < 1$ criterion as suggested by Hajczak et al. [8], where $St = St_D$ or St_W. The tonal peaks are attributed to the noise of the vortex sheddings which are generated on the rounded side of the cylinder, where the radius of curvature is smaller.

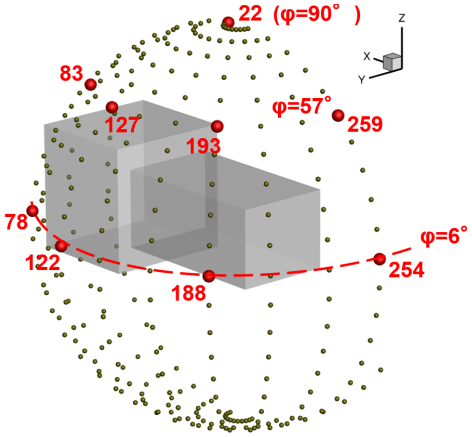

(a) FW-H permeable surface and hemisphere of microphones. The angle ϕ denotes the elevation angle.

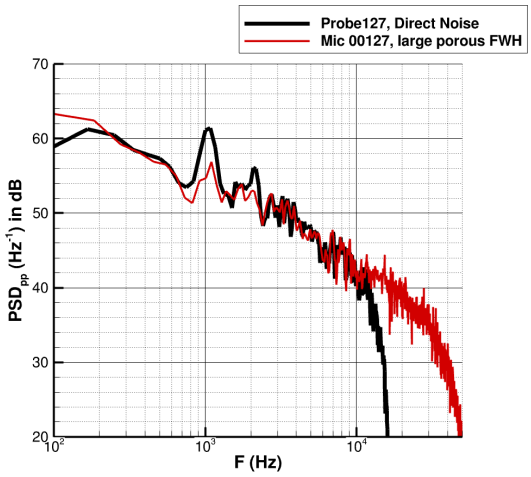

(b) PSD comparison on microphone n°127 for the two acoustic computations.

Figure 5: Aeroacoustics numerical evaluation

Finally, time-resolved acoustic signals are evaluated on two arrays of $M = 369$ microphones arranged around the short cylinder: one positioned horizontally above the cylinder and the other vertically along its side, as illustrated in Fig. 6. The coordinate system is centered at the cylinder, with each array positioned at a distance of approximately $3.3D$ from the origin. Both arrays share an identical geometry, consisting of two perpendicular lines of length $8.4D$, each

containing 185 microphones uniformly spaced by $0.45D$.

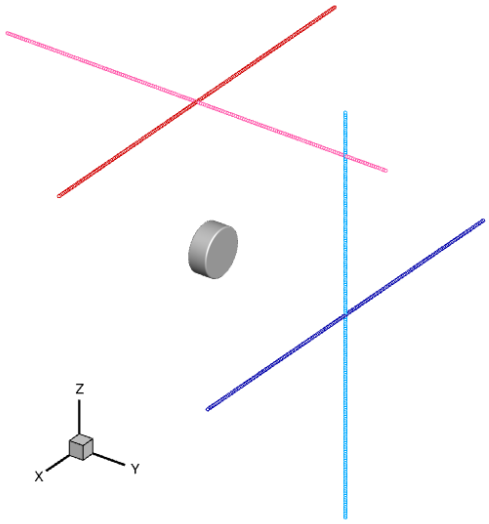

Figure 6: Microphone array setup.

3 ARRAY PROCESSING

3.1 Conventional beamforming

Conventional beamforming remains one of the most popular array processing for sound source localization and quantification. In the Fourier domain, at angular frequency ω, it relies on a linear relationship between the complex-valued vectors $\mathbf{s} \in \mathbb{C}^{I\times 1}$ and $\mathbf{p} \in \mathbb{C}^{M\times 1}$, representing the amplitudes emitted by I uncorrelated sources and the resulting measured data recorded by the M microphones of the array, respectively:

$$\mathbf{p} = \mathbf{G}\mathbf{s} \tag{1}$$

When acoustic propagation occurs within an infinite uniform flow characterized by a low Mach number $M_0 = 0.2$ and a constant sound celerity c_0, the Green's function matrix $\mathbf{G} \in \mathbb{C}^{M\times I}$ must account for the convection of sound waves [16]. From the i^{th} source to the m^{th} microphone, located at positions $\mathbf{x}_i$ and $\mathbf{x}_m$ respectively, the Green's function at wavenumber $k_0 = \omega/c_0$ is given by:

$$G_{mi}(\mathbf{x}_m, \mathbf{x}_i; \omega) = \frac{1}{S}\exp\left(-j\frac{k_0}{\beta^2}\left[S - \mathbf{M}_0 \cdot (\mathbf{x}_m - \mathbf{x}_i)\right]\right), \tag{2}$$

where

$$S^2 = \beta^2\|\mathbf{x}_m - \mathbf{x}_i\|^2 + \left[\mathbf{M}_0 \cdot (\mathbf{x}_m - \mathbf{x}_i)\right]^2 \tag{3}$$

and the Prandtl-Glauert coefficient is defined as $\beta = \sqrt{1 - M_0^2}$.

The initial step involves computing the covariance matrix of the microphone measurements, denoted as $\Gamma \in \mathbb{C}^{M\times M}$, commonly referred to as the Cross-Spectral Matrix (CSM). Welch's method is generally employed to estimate this CSM, ensuring statistical convergence by averaging over K successive snapshots of pressure data:

$$\Gamma = \frac{1}{K}\sum_{k=1}^{K} \mathbf{p}^{(k)}\mathbf{p}^{+(k)} \tag{4}$$

with the Hermitian operator $(\cdot)^+$. Conventional beamforming is subsequently applied by scanning a discrete grid of N focal points covering the region of interest. According to the conclusions of Chardon [6], the acoustic power estimator, denoted by the vector $\mathbf{b} \in \mathbb{R}^{N\times 1}$, is then given by the following relation:

$$\mathbf{b} = \frac{\mathrm{diag}(\mathbf{G}^{+}\Gamma\mathbf{G})}{\|\mathbf{G}\|_2^4} \tag{5}$$

When $\mathbf{x}_n = \mathbf{x}_i$, the ground-truth source power is then accurately recovered. This holds only for the case of a single emitting source. For multiple emitting sources, the result of Eq. (5) can be slightly biased.

3.2 Adaptive beamforming to cross-shaped geometry

When employing a cross-shaped array, Elias proposed modifying Eq. (5) to mitigate strong sidelobes in the acoustic map [7]. This method offers an effective compromise between conventional beamforming, for its ease of implementation and its robustness in adverse environments, and more advanced deconvolution techniques, such as DAMAS or Clean-SC, which require extensive computational resources. The array is partitioned into two sub-arrays, S_A and S_B, with sizes M_A and M_B, corresponding to the microphones along each perpendicular branch. Let $\Gamma_{AB} \in \mathbb{C}^{M_A\times M_B}$ the submatrix of the CSM between these two sets:

$$\Gamma_{AB} = \frac{1}{K}\sum_{k=1}^{K} \mathbf{p}_A^{(k)}\mathbf{p}_B^{+(k)} \tag{6}$$

Using the same logic, the resulting acoustic power estimator writes now:

$$\mathbf{b}_{AB} = \frac{\mathrm{diag}(\mathbf{G}_A^{+}\Gamma_{AB}\mathbf{G}_B)}{\|\mathbf{G}_A\|_2^2\|\mathbf{G}_B\|_2^2} \tag{7}$$

where $\mathbf{G}_A \in \mathbb{C}^{M_A\times N}$ (and similarly $\mathbf{G}_B \in \mathbb{C}^{M_B\times N}$) represents the Green's function matrix restricted to the microphones in S_A (and S_B). Since the submatrix Γ_{AB} is not necessarily positive semi-definite, the matrix products in Eq. (7) may result in negative power values, which are physically invalid, and thus must be set to zero. This beamforming formulation specific to the array geometry, hereafter referred to as adaptive beamforming, provides focusing performance comparable to that of a dense rectangular array of $M_A \times M_B$ microphones in terms of spatial source separation and dynamic range, while employing only $M_A + M_B$ elements.

3.3 Results

At first, acoustic signals generated from the LBM direct noise solution were used to compute the CSM over a small number of $K = 12$ successive blocks, with an overlap of 75% and windowed by a Hanning function. Both the conventional (Eq. (5)) and the proposed adaptive beamforming (Eq. (7)) are applied using the horizontal microphone array located above, along a rectangular focusing grid of $5D \times 2.2D$ and spanning the area around the cylinder with a uniform spatial resolution of approxately $0.5D$ in both directions. Figures 7a and 7b present the resulting acoustic power maps at a single frequency $f = 6$ kHz. In Fig. 7a, the point spread function of the cross-shaped array is clearly visible, and tends to degrade the quality of the source map, as is typically observed with conventional beamforming. In contrast, sidelobe levels are attenuated by up to 10 dB with the proposed adaptive beamforming, thereby improving source identification along the two sides of the cylinder in Fig. 7b. These results are consistent with the fluctuations observed in Fig. 4c.

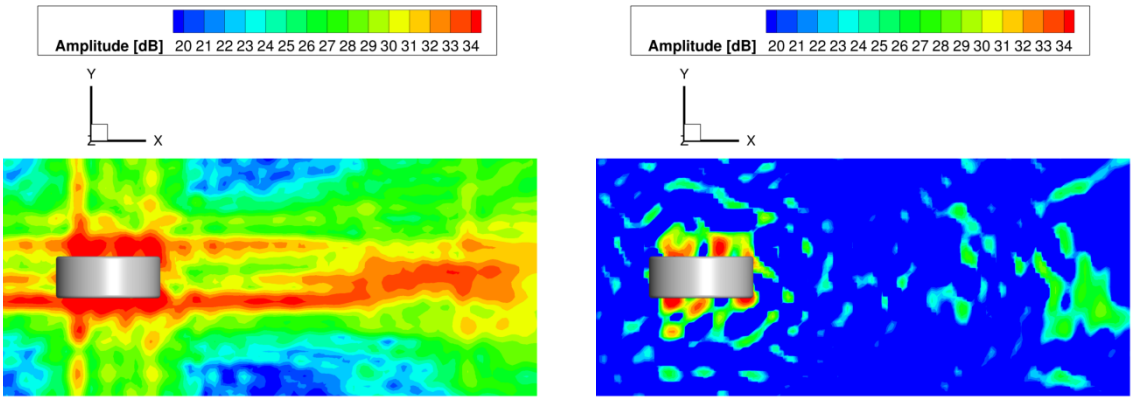

(a) *(b)*

Figure 7: Beamforming maps along a horizontal grid at $f = 6$ kHz using (a) the conventional beamforming and (b) the proposed adaptive beamforming. The CSM is computed using the signals from the LBM direct noise.

Figure 8a and Figure 8b show additional results also at $f = 6$ kHz, obtained with the vertical array positioned laterally to the cylinder, scanning a vertical grid with dimensions and resolution comparable to the previous horizontal grid.

Finally, a comparison between the two CSMs computed using both the LBM direct noise data and the FW-H outputs is presented. Figure 9a and Figure 9b show the resulting acoustic power maps at a frequency of $f = 5$ kHz, obtained only using the adaptive beamforming method. Both appear quite similar in terms of power levels and location of sources near the cylinder. This is expected, as the FW-H integral is directly fed by the LBM flow solution over the permeable surface. In the remainder of the domain, sidelobes are less pronounced when the FW-H outputs is considered. As the FW-H surface integral requires significantly less computational resources than a full high-resolution LBM simulation, a hybrid approach combining both methods is recommended for aeroacoustic source investigation using microphone array processing.

For all the previous Figures, we can note the presence of strong spurious sources downstream of the cylinder along the X-axis. This can be attributed to abrupt transitions at the edges of the

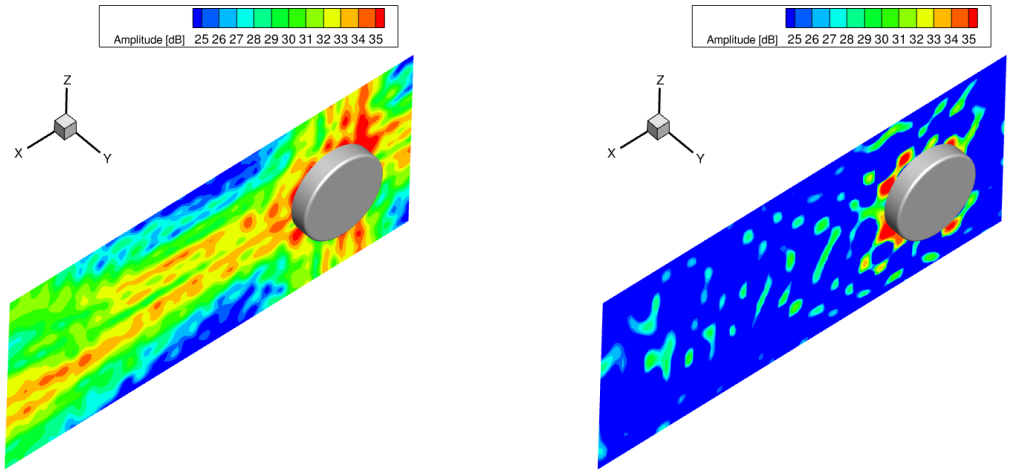

(a) (b)

Figure 8: Beamforming maps along a vertical grid at $f = 6$ kHz using (a) the conventional beamforming and (b) the adaptive beamforming. The CSM is computed using the signals from the LBM direct noise.

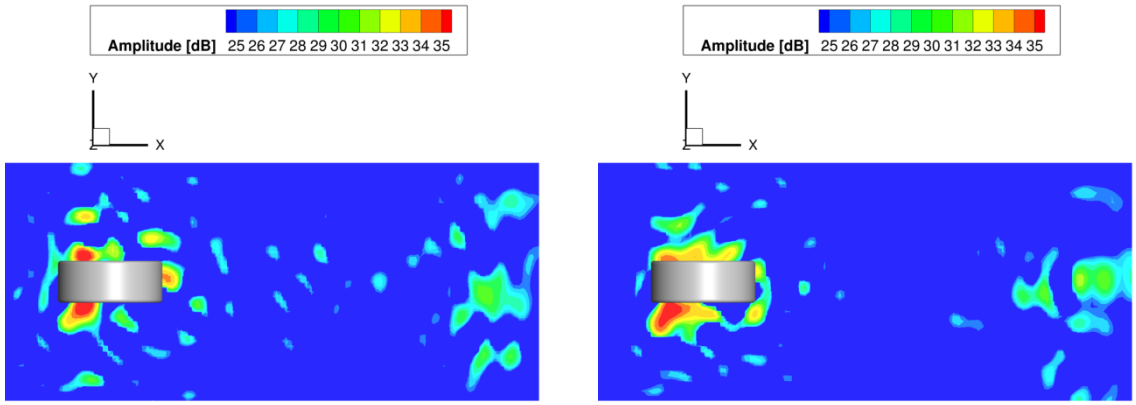

(a) (b)

Figure 9: Adaptive beamforming maps along a horizontal grid at $f = 5$ kHz using the signals from (a) the LBM direct noise and (b) the FW-H permeable surface integral.

meshes, delimited in red in Fig. 2.

4 CONCLUSION

A numerical investigation of the noise generated by a short cylinder, serving as a simplified landing gear wheel, has been conducted. The flow is simulated using the Lattice Boltzmann Method, from which the acoustic propagation is assessed through two distinct approaches: a direct noise computation, and a FW-H integral formulation on a permeable surrounding surface. Comparative analysis of microphone data at mid-field revealed the FW-H outputs provided

superior broadband noise agreement compared to direct noise. An adaptive beamforming technique is then proposed to improve the spatial separation of sources around the wheel, unlike conventional beamforming, while being much easier to implement than other high-resolution algorithms. Applied on synthetic data using two cross arrays located around the cylinder, the results demonstrates its efficiency to capture main acoustic sources around the cylinder.

Future works will focus on simulating noise from arrangments of two or more wheels, in tandem or side by side, to isolate and understand the waves interactions occuring in a realistic landing gear. Also, the introduction of a more complex anisotropic source model, such as dipoles or quadrupoles may prove advantageous in complement of the classical Green's function model. This also involves simultaneously optimizing the focalization grid on the landing gear and the microphone arrays surrounding it, in order to quantify with precision all of its noise-generating mechanisms.

References

[1] N. Afzal. *Wake Layer in a Turbulent Boundary Layer with Pressure Gradient: A New Approach*, pages 95–118. Springer Netherlands, 1996. ISBN 9789400917286. doi:10.1007/978-94-009-1728-6_9.

[2] T. Astoul, G. Wissocq, J.-F. Boussuge, A. Sengissen, and P. Sagaut. "Lattice boltzmann method for computational aeroacoustics on non-uniform meshes: A direct grid coupling approach." *Journal of Computational Physics*, 447, 110667, 2021. ISSN 0021-9991. doi:10.1016/j.jcp.2021.110667.

[3] G. J. Bennett, E. Neri, and J. Kennedy. "Noise characterization of a full-scale nose landing gear." *Journal of Aircraft*, 55(6), 2476–2490, 2018. ISSN 1533-3868. doi:10.2514/1.c034750.

[4] S. Bouley, J. Chambon, and O. Minck. "Enhancement of array processing techniques for caa-based acoustic imaging." In *AIAA AVIATION 2023 Forum*. American Institute of Aeronautics and Astronautics, 2023. doi:10.2514/6.2023-3819.

[5] J. Bulté and S. Redonnet. "Landing gear noise identification using phased array with experimental and computational data." *AIAA Journal*, 55(11), 3839–3850, 2017. ISSN 1533-385X. doi:10.2514/1.j055643.

[6] G. Chardon. "Theoretical analysis of beamforming steering vector formulations for acoustic source localization." *Journal of Sound and Vibration*, 517, 116544, 2022. ISSN 0022-460X. doi:10.1016/j.jsv.2021.116544.

[7] G. Elias. "Source localization with a two-dimensional focused array: optimal signal processing for a cross-shaped array." In *INTER-NOISE and NOISE-CON Congress and Conference Proceedings*, pages 1175–1178. Institute of Noise Control Engineering, 1995.

[8] A. Hajczak, L. Sanders, F. Vuillot, and P. Druault. "A comparison between off and on-body control surfaces for the fw-h equation: Application to a non-compact landing gear wheel." *Journal of Sound and Vibration*, 490, 115730, 2021. ISSN 0022-460X. doi:10.1016/j.jsv.2020.115730.

[9] W. M. Humphreys and T. F. Brooks. "Noise spectra and directivity for a scale-model landing gear." *International Journal of Aeroacoustics*, 8(5), 409–443, 2009. ISSN 2048-4003. doi:10.1260/147547209788549316.

[10] Z. Ivanova, D. Angland, and A. Scotto. "Experimental investigation of reynolds number scaling on the aeroacoustics of a simple landing gear wheel." In *30th AIAA/CEAS Aeroacoustics Conference (2024)*. American Institute of Aeronautics and Astronautics, 2024. doi:10.2514/6.2024-3171.

[11] J. Jacob, O. Malaspinas, and P. Sagaut. "A new hybrid recursive regularised bhatnagar–gross–krook collision model for lattice boltzmann method-based large eddy simulation." *Journal of Turbulence*, 19(11–12), 1051–1076, 2018. ISSN 1468-5248. doi:10.1080/14685248.2018.1540879.

[12] V. Kopiev, I. Belyaev, M. Zaytsev, and K. Zhao. "An aeroacoustic study of full-scale and small-scale generic landing gear models with identical geometry." *Applied Sciences*, 13(4), 2295, 2023. ISSN 2076-3417. doi:10.3390/app13042295.

[13] E. Lévêque, F. Toschi, L. Shao, and J.-P. Bertoglio. "Shear-improved smagorinsky model for large-eddy simulation of wall-bounded turbulent flows." *Journal of Fluid Mechanics*, 570, 491–502, 2007. ISSN 1469-7645. doi:10.1017/s0022112006003429.

[14] E. Manoha, J. Bulté, and B. Caruelle. "Lagoon: An experimental database for the validation of CFD/CAA methods for landing gear noise prediction." In *14th AIAA/CEAS Aeroacoustics Conference (29th AIAA Aeroacoustics Conference)*. American Institute of Aeronautics and Astronautics, 2008. doi:10.2514/6.2008-2816.

[15] A. Suss, I. Mary, T. Le Garrec, and S. Marié. "Comprehensive comparison between the lattice boltzmann and navier–stokes methods for aerodynamic and aeroacoustic applications." *Computers & Fluids*, 257, 105881, 2023. ISSN 0045-7930. doi:10.1016/j.compfluid.2023.105881.

[16] T. Wu and L. Lee. "A direct boundary integral formulation for acoustic radiation in a subsonic uniform flow." *Journal of Sound and Vibration*, 175(1), 51–63, 1994. ISSN 0022-460X. doi:10.1006/jsvi.1994.1310.

[17] K. Zhao, P. Okolo, E. Neri, P. Chen, J. Kennedy, and G. J. Bennett. "Noise reduction technologies for aircraft landing gear-a bibliographic review." *Progress in Aerospace Sciences*, 112, 100589, 2020. ISSN 0376-0421. doi:10.1016/j.paerosci.2019.100589.